To be published in Optics Express:

Title: Referenceless, grating-based, single shot X-ray phase contrast imaging with optimized laser-driven K- sources

Authors: Victorien Bouffetier,Gabriel Perez-callejo,Dan Stutman,Christian Stoeckl,Ildar Begishev,Wolfgang Theobald,Timothy Filkins,Chad Mileham,luke ceurvorst,Sallee Klein,thibault Goudal,Alexis Casner,Maria Valdivia

Accepted: 04 April 24

Posted 04 April 24

DOI: https://doi.org/10.1364/OE.516695

Referenceless, grating-based, single shot X-ray phase contrast imaging with optimized laser-driven K-α sources

V. Bouffetier[1,2,*], G. Pérez-Callejo[3], D. Stutman[4], C. Stoeckl[5], I.A. Begishev[5], W. Theobald[5] T. Filkins[5], C. Mileham[5], L. Ceurvorst[5], S.R. Klein[6], T. Goudal[7], A. Casner[8], M.P. Valdivia[9,10]

[1] *European XFEL GmbH, Holzkoppel 4, 22869 Schenefeld, Germany*
[2] *CELLS- ALBA Synchrotron Light Source, Barcelona, Spain*
[3] *Departamento de Física Teórica Atómica y Óptica, Universidad de Valladolid, 47011 Valladolid, Spain*
[4] *ELI-NP, Institute for Physics and Nuclear Engineering, Bucharest-Magurele 077125, Romania*
[5] *Laboratory for Laser Energetics, 250 East River Road, Rochester, NY 14623, United States of America*
[6] *University of Michigan, Ann Arbor, MI 48109*
[7] *CEA, DAM, DIF, F-91297 Arpajon, France*
[8] *CEA-CESTA, CS 60001, 33116 Le Barp Cedex, France*
[9] *Center for Energy Research, University of California San Diego, San Diego, California, USA*
[10] *Physics and Astronomy Department, The Johns Hopkins University, Baltimore, Maryland, USA*
[*] *victorien.bouffetier@gmail.com*

Abstract:

With its ability to efficiently probe low-Z materials, X-ray phase imaging methods have recently raised high interest in multiple fields from biology and medical applications to high energy density (HED) physics. Initially developed with synchrotron light and X-ray tubes, we present a novel grating based Talbot X-ray deflectometer (TXD) diagnostic which was coupled with laser-generated K-α X-ray sources. The Multi-TeraWatt laser ($I > 1 \times 10^{14}\,\mathrm{W\,cm^{-2}}$) was used as a testbed for diagnostic development. It was found that x-ray source chromaticity plays an important role in TXD. Indeed, the broadband spectrum of laser-generated X-ray sources may strongly impact image quality and thus diagnostic performance. We qualified X-ray emission from different laser-produced sources and determined laser, target, and deflectometer parameters that optimize TXD performance. We present the first results of referenceless grating-based X-ray imaging at high-power laser facilities and discuss the implications of this new development in HED research.

1. Introduction

Since the first demonstration of free propagation X-ray phase contrast imaging with synchrotron source [1], multiple phase imaging based methods have been developed or been transferred toward other X-ray sources [2–5]. These methods can provide enhanced imaging contrast surpassing absorption-based methods when the complex optical index (defined as $n = 1 - \delta + i\beta$) of a medium follows $\frac{\delta}{\beta} \gg 1$ [6]. Therefore, refraction-based imaging methods can enable the characterization of foams [7] in laboratory astrophysics experiments or deuterium-tritium in inertial confinement fusion, for example.

For high energy density (HED) physics, X-ray sources can be generated using high intensity lasers ($I > 1 \times 10^{14}\,\mathrm{W\,cm^{-2}}$) with pulse duration ~ 1 ns interacting with metallic solid samples [8, 9]. Such intense laser-matter interaction enables the generation of hot electrons that can collisionally ionize the K-shell electrons of the metallic sample, thus leading to X-ray radiation, most commonly emitted from the cold K-α line. Depending on the photon energy needed for experimental characterization, different target materials can be laser-irradiated to obtain specific x-ray emission. These laser-generated X-ray sources have demonstrated high potential in single-shot pump-probe experiments in the HED field [4, 10] at facilities such as OMEGA [11], LULI2000 [12], NIF [13] or Laser Mégajoule (LMJ) [14]. However, laser-produced plasmas emit incoherent broadband x-rays with limited flux, which often translates in low signal-to-noise ratio (SNR). As a consequence, optimizing X-ray backlighters is necessary to obtain high contrast X-ray radiographs.

The optimization of the emissivity of K-α laser-generated X-ray sources is necessary to provide sufficient photon statistics for high resolution X-ray radiographs but also to overcome the X-ray background surrounding the irradiated targets to be imaged. Typically, the lifetime of a laser produced X-ray source corresponds to the duration of the laser pulse used to generate it. Therefore, even with pulse duration of the order of 100 ps, the spatial resolution of radiographs can be limited to a few microns by the motion blur only. Additionally, the K-α emission is also usually accompanied by a strong continuous bremsstrahlung emission. Each wavelength emitted from the source contributes therefore to the final image, thus degrading the resolution due to chromaticity. The last potential issue to face with laser X-ray generated sources is the size of the source itself: the larger the source, the lower the resolution. To diminish the effective source size, one may make use of pinholes to enhance the resolution of the radiographs. However, this solution comes to the cost of available photons for the radiography.

In this paper, we study different backlighter configurations for grating-based Talbot-Lau X-ray interferometry, a refraction-based imaging method, at the MTW laser [15]. This grating based imaging diagnostic makes use of the Talbot effect [16], which consists on the self-imaging of a periodical object at particular planes, known as Talbot planes, when illuminated by coherent [17] or partially coherent light [18]. In the presence of incoherent sources, such as those produced by the aforementioned laser-generated X-ray sources, the Talbot-Lau imaging technique relies on the Lau effect [19] to enable X-ray interferometry with initially spatially incoherent light. In this case, an additional grating is used to provide a collection of partially coherent sources, which enable the formation of the fringe pattern [3].

Talbot X-ray Deflectometry (TXD) allows for independent transmission and phase change measurements from Fourier analysis [20, 21] of the interferometric pattern. Obtaining ion density from X-ray attenuation signals retrieved with TXD is equivalent to standard absorption radiography. The electron density from a sample can thereafter be unveiled by measuring refraction angles from the changes of the interferometric pattern [22, 23]. The possibility to measure strong electron density gradients is highly relevant to the characterization of a wide range of HED plasma phenomena which are critical for the benchmark of theoretical and numerical models such as heat transport, turbulent diffusion coefficients, or self generated B fields [24, 25]. However, to quantitatively evaluate the phase-shifts induced by a sample to a X-ray wavefront, acquiring a reference image of the unperturbed interferometric pattern is necessary, since the fringes shift due to the presence of a refracting sample even if it is unperturbed.

In this type of experiments, x-ray source brilliance and photon flux are usually limited by a number of experimental factors that lead to low SNR, making interferometry data analysis and phase retrieval challenging [26, 27]. Nevertheless, accurate phase retrieval has been demonstrated using a different x-ray backlighter source to record reference images [28]. Recently, Pérez-Callejo *et al.* [21] successfully retrieved a differential phase map from a low SNR Moiré image and a set of reference images recorded through phase-stepping methods [29]. This technique has shown enhanced resolution and contrast capabilities when compared to single-shot Moiré and thus, reference image recording through phase-stepping is a viable alternative for high-power laser facilities. However, phase-stepping procedures can be time consuming and thus incompatible with next generation high repetition rate facilities such as in ELI-beamlines [30] and XFEL

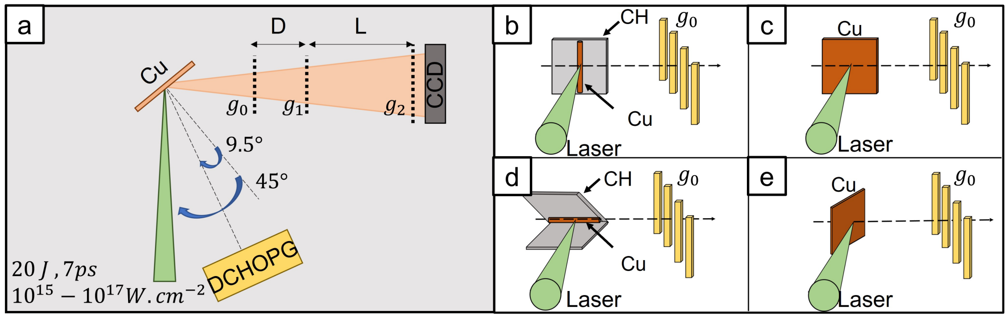

Fig. 1. (a) Experimental setup used for x-ray backlighter studies for Talbot-Lau X-ray Deflectometry imaging diagnostics performed at the MTW laser. DC-HOPG spectrometer orientation shown with respect to Cu foil target irradiated at 45°. Backlighter target orientation is shown for each type explored: (b) Cu wires with CH foil backing, (c) Cu flat foil irradiated at 90°, (d) bookend configuration: Cu wire in between two CH flat foils, and (e) Cu flat foil irradiated at 45°.

facilities [31].

Our study addresses this challenge by self-estimating the phase background from sample interferograms instead of acquiring separate reference images. This method simplifies the experimental imaging procedure with a Talbot-Lau interferometer since no reference or phase-stepped data set is needed and closer matches the operation procedures at laser facilities. To enable referenceless Talbot-Lau X-ray phase contrast imaging, it is mandatory to have a clear signal. While the X-ray imaging conditions would be easier fulfilled at XFEL facilities [32–34] due to their sharp spectrum and extreme brilliance [35], we aim here to demonstrate the feasibility of such imaging methods within a single shot at high power laser facilities where the X-ray sources generated by laser will provide broader X-ray spectra and lower brilliance. Therefore, it is mandatory to optimize both the emission lines and the flux of the laser-driven X-ray sources to improve these aspects to enable single-shot Talbot phase contrast imaging at high power laser facilities.

This paper is structured as follows. The details of the Talbot-Lau interferometer and X-ray backlighter targets used at the MTW laser are presented in Sec.2. In Sec.3, we analyze the spectra from different laser-produced x-ray sources and their brilliance. The quality of TXD fringe patterns was evaluated considering the X-ray backlighter source characteristics in Sec.4, which are correlated to the backlighter target type. The last section presents x-ray transmission and phase map reconstruction of a polymethyl methacrylate (PMMA) rod, using TXD imaging where no reference image is available. Single-shot TXD acquisition mode is discussed and compared to absorption radiography methods currently available at high-power laser facilities.

2. Experimental setup at MTW laser

2.1. Talbot-Lau setup

The Talbot-Lau interferometer used in this study (Fig.1) is composed of 3 gratings. The source, beamsplitter and analyzer gratings (hereafter referred to as g_0, g_1 and g_2 respectively). The g_0 grating had a pitch of $p_0 = 2.4\,\mu$m and its purpose is to generate partial spatial X-ray coherence [6, 36] following the Lau effect. The g_1 grating was a π-shift grating with a pitch of $p_1 = 3.85\,\mu$m. This grating was used as the self-imaging Talbot object. Finally, g_2 had a pitch of $p_1 = 3.85\,\mu$m, and was used to perform spatial filtration before the detector.

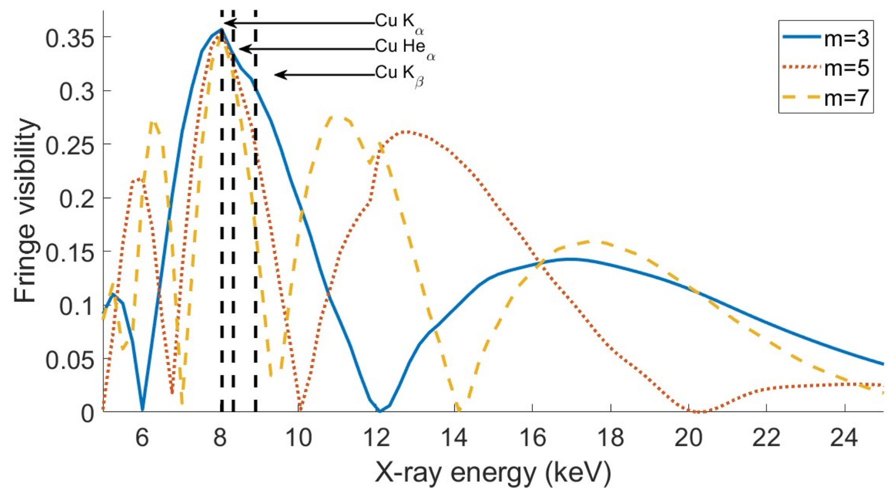

Fig. 2. Interferometer fringe contrast curves for the 8 keV Talbot-Lau X-ray Interferometer calculated with the X-ray WaveFront Propagation (XWFP) code [37] as a function of X-ray wavelength for three different Talbot orders.

The Talbot planes produced by the π-phase grating g_1 are located at the positions:

$$L = m\frac{p_1^2}{8\lambda}, \tag{1}$$

where $\lambda = 1.54$ Å (i.e. 8 keV photon energy) is the X-ray wavelength used in the experiment, and the Talbot order m is an odd number for π-shift phase gratings [36]. Our system was designed to work in the $m = 3$ order.

To optimize the signal quality delivered by the diagnostic, the distances between gratings must follow the Lau conditions to enable X-ray diffraction [28]:

$$\frac{p_0}{p_2} = \frac{D}{L}, \tag{2}$$

where D is the $g_0 - g_1$ distance. The divergence of the X-rays and the splitting introduced by the g_1 grating produce a magnification of the Talbot diffraction pattern. At the position of g_2, the Talbot magnification can be expressed as:

$$M_T = \frac{L + D}{D}, \tag{3}$$

Note that Talbot magnification must be taken into account when re-scaling Talbot distances [36].

To minimize grating ablation due to driver laser proximity, an $M_T = 6$ magnification was used. In this case, the $g_1 - g_2$ distance re-scales as:

$$L = 3M_T\frac{p_1^2}{8\lambda} = 21.66\,\text{cm}, \tag{4}$$

which considers the $m = 3$ Talbot plane and the π-shift behavior of the beam-splitter g_1. Thus, the $g_0 - g_1$ distance is fixed to $D = 4.67$ cm according to Eq.2.

Additionally, the phase grating was rotated $\theta_M = 0.3°$, producing Moiré patterns with periodicity given by:

$$P = \frac{p_1}{2sin\left(\frac{\theta_M}{2}\right)} = 735\,\mu\text{m}. \tag{5}$$

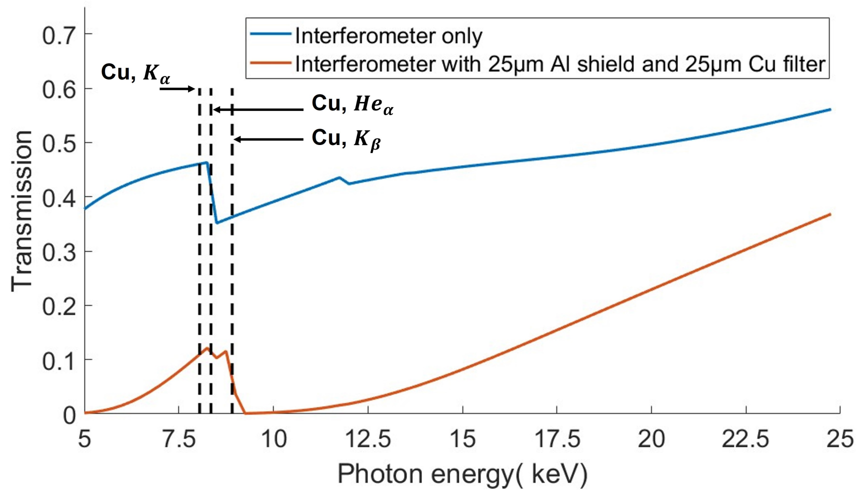

Fig. 3. X-ray transmission curves for TXD diagnostic (blue) obtained with XWFP. A second transmission curve (red) includes a 25 μm Al foil and a 25 μm Cu foil to account for the source grating protective shield and the CCD camera detector filter, respectively.

Note that the acceptance bandwidth to optimize the fringe contrast is also restricted [38]:

$$\delta\lambda = \frac{\lambda_0}{2m-1} \approx 0.3\,\text{Å}, \tag{6}$$

The interferometer was designed to operate at $\lambda_0 = 1.54$ Å (i.e. 8 keV photon energy), the main copper K-α wavelength. Consequently, it is necessary to optimize X-ray flux from Cu K-shell emission between 1.84 Å and 1.24 Å (or 6.74 keV to 10 keV).

Fig.2, shows XWFP [37] interferometer contrast calculations for the 8 keV TXD diagnostic system as a function of X-ray energy, showing three different Talbot orders. It is clear that the bandwidth of the main peak ($\sim$ 8 keV) becomes narrower with increasing Talbot-order (in accordance to the first-order approximation in Eq. 6).

Considering the above, the optimization of x-ray emission from the copper backlighter for TXD diagnostics focuses mainly on the K-α and He-α emission lines. In our experiments, copper targets of different geometries were explored. Since variations in laser intensity and laser-matter interaction determine which atomic processes are dominant, different laser parameters such as energy, spot size on target, and pulse duration were explored.

An 25 μm aluminum debris shield was placed in front of the source grating. A 25 μm copper filter was placed in front of the X-ray CCD camera to filter low energy emission and protect the detector from debris and stray light. The total transmission of the Talbot-Lau diagnostic with its shields and CCD filters was $T_T \sim 10\,\%$ for a photon energy of 8 keV, supported by previous experiments [39] and theoretical calculations, shown in Fig.3. While photon energies below 8 keV are minimized, x-ray transmission above 12.5 keV is significant and may impact diagnostic quality.

2.2. Experimental geometry at MTW laser

In this MTW laser experiment, laser intensity was varied between 1×10^{15} W cm^{-2} and 7×10^{16} W cm^{-2} with pulse duration of $\tau = 7-11$ ps and energy of $E_{laser} \approx 11-28$ J [40]. Most shots were performed at $\tau = 7$ ps and $E_{laser} = 25$ J. On-target intensity was varied by modifying laser spot on target from 75 μm to 251 μm. TXD images were recorded using single shots. It is worth noting that the MTW laser usually provides no more than 11 shots per day for this type of experiments.

The distance between the X-ray source (i.e., backlighter target) and the g_0 grating was set to 4 cm to minimize grating damage from backlighter target debris. The angle between laser incidence and diagnostic line of sight was 90°. The Moiré fringe pattern was recorded with an Andor iKon-L X-ray CCD (1024x1024 pixels of 13 μm) placed behind the g_2 grating.

To quantify x-ray backlighter emission and flux at 8 keV, a dual-channel highly-oriented pyrolytic graphite (DC-HOPG) [41] was used to monitor spectra in the 7 − 10 keV range. Lower energies were filtered with Al and Cu foils, as described above. It is worth noting that no information was available for emission above 10 keV. Due to vacuum chamber geometry restrictions, the angle between DC-HOPG and TXD line-of-sight was 54.5°, as shown in Fig.1. This determined the spectrometer to backlighter target angle.

In order to optimize the backlighter radiation, we tested six different target geometries. Table 1 lists backlighter target type and orientations tested. The main backlighter targets used were Cu foils oriented at 45° with respect to TXD line-of-sight (Fig.1.e). Different foil thickness were tested. Foil targets were also set normal to laser incidence (i.e., along TXD optical axis), as shown in Fig.1.c. Copper wire targets (20 μm diameter) were tested either with flat plastic foils backing (Fig.1.b) or along the side of two plastic foils set at angle in the shape of an open book (Fig.1.d), also known as bookend targets [42].

Backlighter type	laser incidence
$200 \times 200 \times 20\,\mu$m Cu foil	45°
$200 \times 200 \times 12.5\,\mu$m Cu foil	45°
$200 \times 200 \times 20\,\mu$m Cu foil (edge on)	90°
$200 \times 200 \times 12.5\,\mu$m Cu foil (edge on)	90°
CH backed 20 μm wire	90° (to CH foil)
Bookend	90°

Table 1. Backlighter types and orientation

2.3. Spatial resolution

With plane wave illumination, the maximum resolution of a Talbot-Lau interferometer is equal to two times the period of the analyzer grating [38]. For spherical waves, the grating transmission function has to be considered for back-propagation at the object plane. For the TXD configuration presented in Figure 1 the object was placed at a distance $p = 3.2$ cm from g_0, leading to a back-projected period of the analyzer grating of $p_2' = p_2 \frac{p}{L+D} = 1.46\,\mu$m. This yields a maximum theoretical resolution is 2.92 μm. This limit in the spatial resolution of the interferometer assumes an ideal punctual X-ray source which, as mentioned before, is not usually the case when working with laser generated X-ray sources. With extended X-ray sources, the on sample spatial resolution with a Talbot-Lau interferometer is given by [3]:

$$r = s\frac{L}{D}, \tag{7}$$

where s is the X-ray source size.

It has been observed in the literature that the size of a laser-generated X-ray sources is generally two to four times larger compared to the laser's on target spot size [43, 44] due to the plasma expansion of the source. Similarly, for wire targets we assume that the source size is around 3 times the wire's diameter ($s \approx 60 \mu m$) thus leading to improved source size compared to foil targets [45]. Making use of Eq.7, the best effort resolution achievable with our interferometer corresponds to wire backlighters and is $r \approx 12\,\mu$m.

Another limitation to take into account arises from the detector. For our images, we used 2×2 binning, i.e., an effective pixel size of $s_{p,e} = 26\,\mu$m. With a Talbot magnification $M_T = 6$ (cf. Sec.2.1), the best effort resolution from the detector is $r_d = \frac{s_{p,e}}{M_T} = 4.3\,\mu$m. With the additional consideration that photon energy may spread over pixel neighbours, the maximum resolution resolvable by the detector is then estimated to be close to $12\,\mu$m in this configuration. Therefore the 2×2 binning corresponds to the optimal recording setting to match the interferometer resolution.

2.4. Benefits of Talbot-Lau interferometry in high-power laser facilities.

As mentioned in Section 1, propagation-based phase-imaging methods have been successfully demonstrated in laser facilities [4]. Nevertheless, due to large source size and incoherence of laser-generated X-ray sources, long propagation distances are needed to distinguish phase related intensity changes at the imaging plane, often above one meter [46]. This restriction leads to low photon flux and, since intensity variations depend on the second derivative of the wavefront phase [47], these techniques are usually less sensitive than grating-based phase-contrast methods [3, 48].

Talbot-Lau X-ray interferometers can be made compact and compatible with high-power laser facilities. Interferometry requires coherence length $L_\perp$ to be sufficiently large compared to the interferometer's shear length L_S, i.e., $\frac{L_S}{L_\perp} < 1$. The shear length in Talbot-Lau interferometry is given by $L_S = \frac{(m - \frac{1}{2})}{M_T} p_1$. In our case, $m = 3$ with $L_S = 1.60\,\mu$m, and lateral coherence length becomes $L_\perp = \frac{\lambda D}{p_0} = 2.99\,\mu$m [36, 38].

The best focusing effort in our experiment enabled a spot size of $75\,\mu$m. To at least conserve the $\frac{L_S}{L_\perp}$ ratio obtained with our diagnostic, the propagation distance between the X-ray source and the g_1 phase grating would need to be increased significantly if no source grating or pinhole is to be used. Talbot-Lau interferometry is therefore a good compromise between sensitivity and diagnostic compactness.

3. Spectral analysis and X-ray source comparison criteria

3.1. Spectral analysis of the backlighter

The number of photons emitted in 4π sr can be retrieved from spectra signal S_m using [49]:

$$S = 4\pi \frac{S_m \eta_{CCD}}{Q_E T_{filter} \Omega}, \tag{8}$$

where Q_E is the detector quantum efficiency, T_{filter} is the combined filter transmission in the desired energy range, $\eta_{CCD} = 4.25 \pm 0.3\,\mathrm{eV/ADU}$ is the characteristic response of the detector, and Ω is the solid angle emitted by the source that reaches the spectrometer detection area.

Fig.4, shows DC-HOPG spectra in the $7 - 10\,$keV energy range for the backlighter targets tested. K-α emission is enhanced when using $20\,\mu$m foils, with a slight increase for normal laser incidence. At 45° angle, higher continuous background emission is observed, which may decrease interferometer contrast (Fig.2). Both types of wire targets offered lower K-α flux due to the lower cross section between the laser spot and copper surface.

From these results, it may seem that foils irradiated at normal incidence offer the best X-ray backlighting conditions for TXD, producing lower continuous emission and higher photon flux, increasing Moiré fringe visibility and optimizing diagnostic accuracy. Considering that the interferometer has low transmission below 8 keV, contrast decrease can be attributed to harder

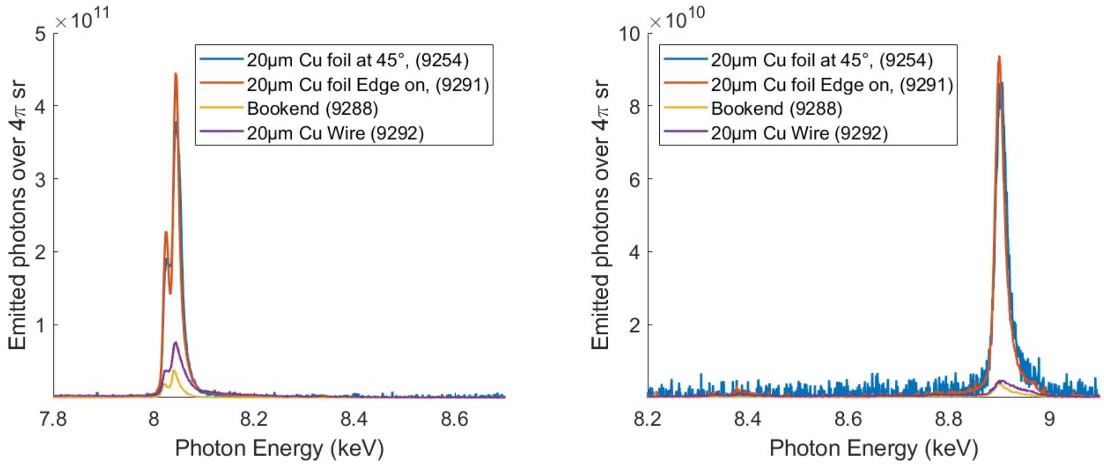

Fig. 4. Spectra recorded by DC-HOPG spectrometer corresponding to the different backlighter configurations irradiated with a laser intensity of $1 \times 10^{15}\,\mathrm{W\,cm^{-2}}$. The Low energy channel (7.8 - 8.5 keV) is shown on the left and the High energy channel (8.2 - 9.15 keV) is shown on the right.

X-rays ($\epsilon_{photon} \geq 12\,\mathrm{keV}$) [50]. Moreover, the effects from these energy contributions can be measured directly from Moiré fringe pattern and SNR.

Nevertheless, although the wire targets provide lower X-ray flux, these targets were still considered as they may provide enhanced spatial resolution when compared to foils [45].

3.2. Conversion efficiency

Laser to K-α conversion efficiency (ϵ_{conv}) is a relevant criterion to compare x-ray backlighter photon flux obtained for a given laser intensity. This coefficient can be expressed by:

$$\epsilon_{conv} = \frac{E_{K_\alpha}}{E_{laser}}, \tag{9}$$

where E_{K_α} is the total energy irradiated in the K-α range by the X-ray source, and E_{laser} is the total energy contained in the laser pulse [49]. This conversion efficiency factor measures our ability to convert laser energy to X-ray energy irradiated under the form of 8 keV K-α emission for the various backlighter configurations tested.

Fig.5 shows the K-α conversion efficiency and average value (dotted line) measured for each backlighter target configuration at different laser intensities. Note that photon flux trends (Fig.4) agree with those observed for conversion efficiency, indicating higher percentage of laser energy converted to K-α emission from flat foils in comparison to wire targets.

Remarkably, the conversion efficiency of foils is nearly an order of magnitude higher than for wires. Lower conversion efficiency is attributed to the laser spot being larger than the wires, and therefore only a small fraction of the laser energy is deposited on the wire and can be converted to X-rays. This is therefore a strong limitation in the conversion efficiency from laser to K-α photons when using large laser spots compared tot the wire diameter.

In Fig.5, the error bars correspond to the standard deviation of the mean photon production for a given backlighter configuration and laser intensity reproduced 3 times. The larger error bars obtained for wire targets can be explained by jitter related to target area irradiated. Similarly, random speckle pattern in the laser spot can contribute to non-uniformity in the laser intensity distribution within the target area irradiated, leading to large shot-to-shot fluctuations. While

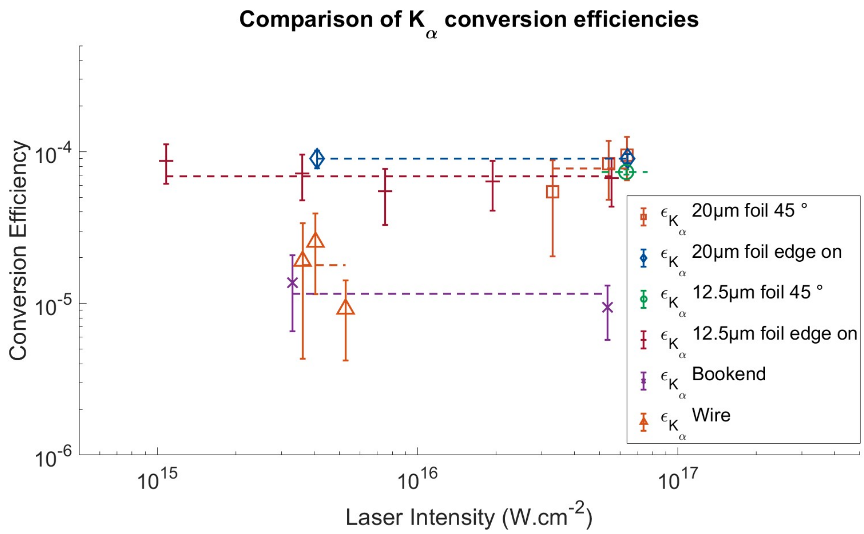

Fig. 5. Conversion efficiencies for K-α emission measured for each backlighter target configuration as a function of laser intensity. Conversion efficiencies for copper foils of 12 μm and 20 μm thickness irradiated at 45° and at normal incidence are shown along with 20 μm diameter copper wire targets backed by either a single CH foil or two adjoined CH foils in the bookend configuration.

wire targets generate smaller X-ray sources, their suitability for TXD diagnostics is hindered by laser jitter effects which are accompanied by lower conversion efficiency.

Note that non-uniformity effects are less important when irradiating foil targets as they offer a larger interaction region, which is consistent with the results obtained. Copper foil targets show increased photon flux and foil thickness of 20 μm nearly doubles the conversion efficiency of 12.5 μm. Moreover, due to laser pointing and target alignment fluctuations, K-α conversion efficiency is similar for normal and 45° laser incidence considering the error bars.

3.3. Brilliance of the laser-generated X-ray sources

X-ray brilliance enables quick comparison between different X-ray sources in terms of spectral bandwidth. It is defined as

$$\mathscr{B} = \frac{\dot{N}_{phot}}{S \cdot \Omega \cdot 0.1\% BW}, \tag{10}$$

where $BW = \frac{d\omega}{\omega}$, S is the source size, Ω is the source divergence Ω and $\dot{N}_{phot} = \frac{dN_{phot}}{dt}$ is the photon fluency. Brilliance is generally given in units of photon/s/mrad^2/mm^2/0 1%BW [35]. In the case of pulsed X-ray laser-generated sources, peak brilliance provides better insights because it only takes into account the X-ray source parameters over the short lifetime of the X-ray source which is about the laser pulse duration (instead of using time derivative of the emitted photons).

As mentioned above, TXD methods are independent from the X-ray source size (since the effective source size is given by g_0. For this reason, the easiest way to enhance the brilliance of our X-ray source is to optimize photon flux by finding backlighters with optimal conversion efficiency.

Fig.6 shows the estimated peak brilliance for each backlighter type as a function of laser intensity. Source brilliance increases with intensity as a consequence of larger energy and stronger focusing. For these estimations, the bandwidth of the K-α source is taken equal to the width of the K-α peak, $\sim$ 100 eV divided by the K-α photon energy $\epsilon_{K-\alpha} = 8.05$ keV. Given that

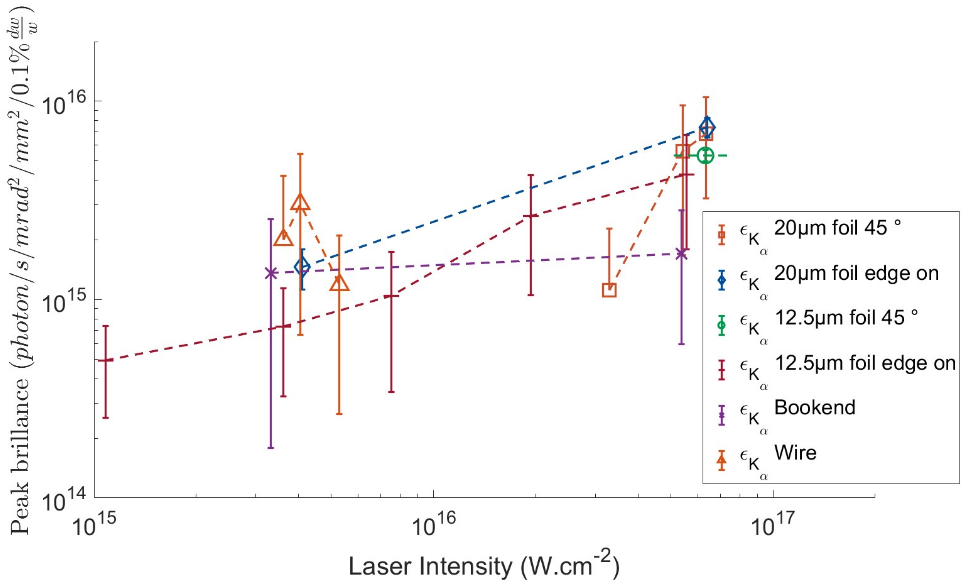

Fig. 6. (a) Estimated peak brilliance of the laser generated X-ray sources depending on the laser intensity and irradiated backlighter. (b) Zoom in the dense region of experimental points of brightness.

the generated plasma emits X-ray in all directions, the divergence of the X-ray source has been taken to be $\Omega = 4\,\pi$sr.

In our experiment we did not have any imager to measure precisely the size of the X-ray source. Nevertheless, the literature shows that the size of the X-ray source is generally about 2-4 times larger than the cross-section between the backlighter surface and the laser spot [43–45]. For this reason, we used an average source size value of 3 times the cross-section between the backlighter surface and laser spot. Nevertheless, we are including the uncertainty in the source size in the error bars of Fig. 6.

For intensity $I = 1 \times 10^{15}$ W/cm^2 to 1×10^{16} W/cm^2, wire backlighters have brilliance similar to foils. Thus, the use of wire targets is of interest within the laser intensities explored, showing potential advantages over foil targets which is yet to be confirmed for a larger intensity range according to the presented data set.

4. Imaging results

4.1. Backlighters impact on the Talbot pattern formation

Fig. 7 shows the TXD images recorded using x-ray backlighting from: copper foil (top) irradiated at 45° (left) and normal to the laser (right), and copper wire (bottom) backed with a single CH foil (left) and a double CH foil in the bookend configuration (right).

The fringe contrast measured from the Talbot pattern is highly dependent on the x-ray backlighter brilliance. The phase contrast curve shown in Fig.8 was obtained by averaging intensity over twenty-five pixels. The highest contrast measured (31 %) corresponds to a Cu wire target. Cu foil targets delivered fringe contrast of 20 − 30 % and bookend targets delivered 19 % contrast. The latter is explained by higher ratio of continuous background radiation to K-α emission when compared to Cu foils and CH-backed Cu wires.

Considering imaging quality, CH-backed Cu wires are the most suitable backlighter targets for high contrast TXD diagnostic accuracy. The X-ray sources produced by these targets achieve a

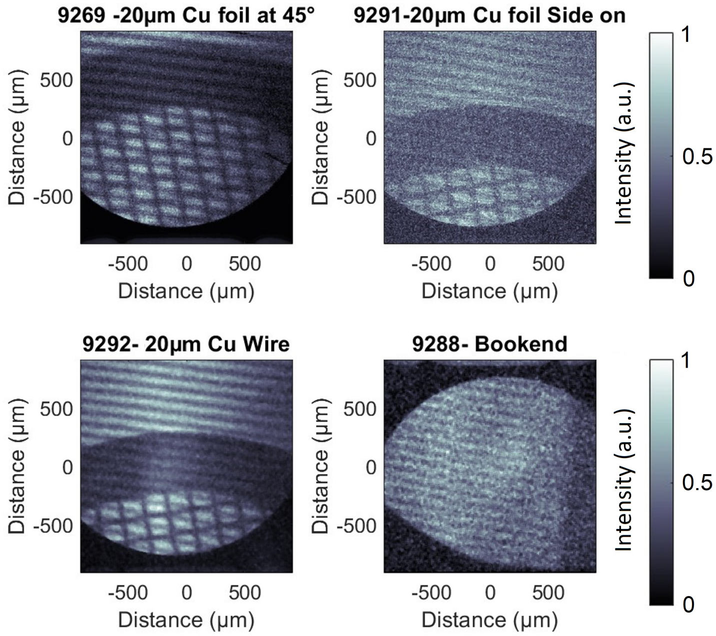

Fig. 7. Talbot radiographs (Moiré deflectograms) recorded using x-ray backlighter emission from the different target configurations tested. Pictures shown have median filtering of 3x3 pixels.

higher spatial resolution due to higher brilliance at laser intensity $I = 4 \times 10^{15}$ W/cm^2. However, the reduced backlighter target area is a challenge for laser focusing. As mentioned previously, this can lead to high variablility in K-α conversion efficiency and total photon flux production, including various levels of associated noise. In extreme cases, spectrum broadening may occur if the laser partially irradiates the target stalk. Recall that broad spectrum decreases contrast due to the chromaticity dependance of the interferometer, which will lead to the absence of Moiré fringes.

Note that the larger spatial extent of flat foil targets ensures that the x-ray spectra obtained will correspond to copper emission exclusively. Therefore, flat foil targets offer better x-ray production and reproducibility shot to shot. Moreover, for the laser incidence angles tested (45° and 90°) target alignment is easier to perform with regards to the facility constraints.

Moiré fringe quality for Cu wire backlighters is comparable to 45° Cu foil with lower production of X-ray photons. This is a direct illustration of the importance of enhanced brilliance considering working intensity of 4×10^{15} W/cm^2 (Fig.6). That is, with copper foils targets, one can rely on higher photon statistics, and with wires, one can rely on higher brilliance.

4.2. Toward single-shot referenceless phase imaging

The raw Moiré image of a PMMA rod recorded using a copper wire backlighter target is shown in Fig. 9.**a**. Wire backlighter have been chosen here due to the enhanced fringe contrast they can provide as shown previously. The fringe pattern perturbation produced by the X-rays passing through the rod is clearly observed at the edges of the rod. Through Fourier analysis of the signal, the phase and transmission information can be retrieved from this pattern. In these studies, the analysis was performed using the Talbot Numerical Tool (TNT), a sub-module of the Talbot

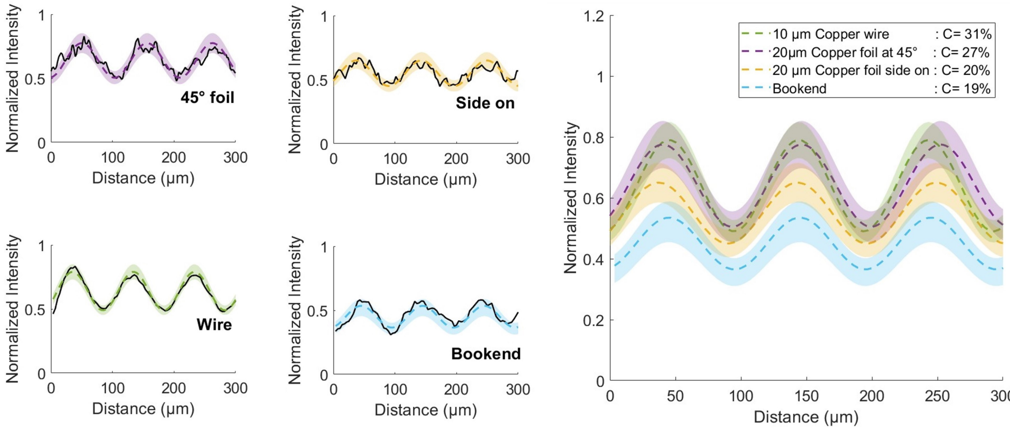

Fig. 8. Moiré fringe profiles obtained for the backlighter target configurations studied: flat foils irradiated at 45° and 90°, wires, and bookends. The average of the raw intensity signal is shown in solid black line, the profile fit is shown as a dashed line, and the corresponding error is shown as colored area.

Interferometry Analyzer (TIA), which has been developed by our team and described in previous publications [20, 21].

The analysis was performed as follows. We first obtained the phase and transmission images of the PMMA rod (750 μm diameter) placed between the source and phase gratings. By using a high-quality backlighter from the different sources studied in this work, we ensured a high-quality fringe pattern. Therefore, we can assume an ideal reference image, that is, a flat mean illumination and a linear phase following the unperturbed fringe pattern. This allows us to retrieve the transmission and phase changes induced the PMMA rod. It should be noted that the limitation of this method reposes on the characteristics of the gratings. If any of the gratings used in the interferometer have structural defects that affect their pattern or periodicity, accuracy will be compromised as this methods assumes uniform and ideal reference. Therefore, defects from the instrument transmission function will be conserved in the final image.

The transmission and differential phase maps obtained are shown in Fig.9.**b** and **c**, respectively. The non-uniformities observed in these images arise from the phase unwrapping process, which is highly sensitive to noise. The noise associated to the raw Moiré TXD image is caused by the broadband properties of laser-generated X-ray sources.

Fig. 9.**d** shows a line-out of the transmission image Fig.9.**b**, compared with the theoretical transmission of a cold PMMA rod. The differences between the red and yellow theoretical lines arise from the spatial resolution and including the polychromaticity of the spectrum.

Fig. 9.**e** shows the refraction angle induced by the rod computed from the differential phase image. This refraction angle is obtained from the measured fringe shift $F = \frac{\phi}{2\pi}$ and the angular efficiency of the diagnostic $W_{eff} = \frac{p_0}{l}$. The denotation ϕ is the signal's phase, $p_0 = 2.4\,\mu$m the periodicity of the source grating, and $l = 3$ cm is the distance between g_0 and the PMMA rod. The experimental measurement is compared to a theoretical curve computed using the XWFP code. This curve has been blurred by a 12 μm FWHM gaussian to account for image resolution as described in Sec.2.3.

The most important merit of the work presented is that no reference image has been used to retrieve the phase and transmission information from the raw Moiré image shown in Fig.9.**a**. As mentioned in the introduction, standard interferometry diagnostics require an object and a reference image to obtain the absolute phase change by accounting for the background phase

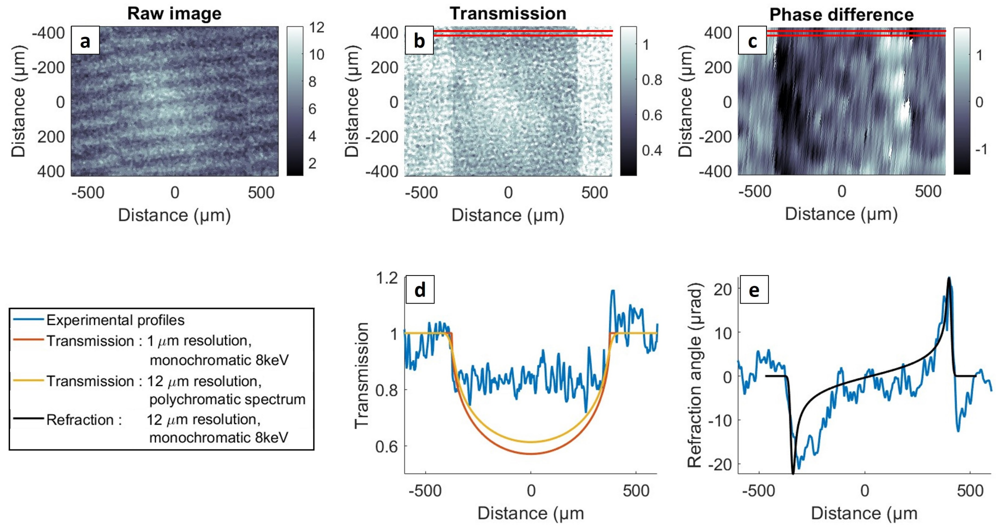

Fig. 9. Phase retrieval process through single-shot referenceless TXD imaging. (a) Moiré deflectogram of a 750 μm diameter PMMA rod. (b) Transmission image retrieved with TNT tool. (c) Phase image obtained from Fourier analysis of the fringe pattern. Transmission (d) and refraction angle (e) line profiles for the PMMA rod, both theoretical and experimental. The resolution of the theoretical curve is 12 μm following the results in Sec.2.3. The line-out profiles in (d-e) were obtained for the region between the 2 red lines shown in the figure to avoid the brighter region observed in the center of the image. This area corresponds to a 23 μm integration region.

associated to the X-ray wavefront. By optimizing the backlighter properties, the signal quality and fringe contrast is significantly increased, which allows for single-shot imaging in similarity to standard radiography methods.

Notably, since the number of laser shots in an experimental campaign is limited at high-power laser facilities, referenceless Talbot-Lau X-ray phase contrast imaging represents an important advantage as it can provide transmission and refraction information in a single shot. Moreover, it has been recently demonstrated that ex-situ phase-stepped Moiré references can be recorded immediately before laser shots on the OMEGA-EP laser [21]. Considering that phase-stepped images can be time costly and require additional diagnostic preparation and support, referenceless imaging could present a viable and reliable option for Talbot X-ray phase contrast diagnostics.

5. Conclusions and future work

X-ray phase contrast imaging is a valuable tool to extend the information obtained from single-shot radiography in pump probe experiments. Measuring the phase with accuracy is a mandatory step to retrieve meaningful information on more complex dynamics in laser-generated plasma systems. Talbot X-ray deflectometry is a promising diagnostic method to probe dense laser-generated plasmas due to higher penetration of X-rays when compared to optical light. With the ability to probe ion and electron density in a single shot, this diagnostic is therefore a valuable tool for future studies of transport, diffusion coefficients, turbulence and more generally for laboratory astrophysics and ICF.

We have demonstrated the importance of X-ray source development as it strongly impacts diagnostic accuracy through imaging quality. The study here presented focused on foil and wire targets in standard X-ray backlighter configurations found at high-power laser facilities.

The development of copper K-α X-ray sources was the main focus considering a single 8 keV Talbot-Lau Interferometer design. It was found that optimization of either X-ray flux or X-ray source brilliance is possible, where flat copper foils oriented at normal incidence generate higher X-ray flux while wires deliver higher brilliance, enabling high fringe contrast of the order of $\approx 30\,\%$. Since X-ray backlighter flux shall overcome self-emission from the probed plasma object, normal incidence on copper foils may be preferred in high-power laser experiments. In materials science or biological applications, where laser-generated X-ray sources can also find interest, wire targets may be of interest considering the smaller X-ray source size and higher brilliance provided. Further, a good compromise between X-ray source flux and brilliance could be reached in irradiating a planar metallic foil coupled with a pinhole aperture [51, 52] or micro-dot targets [53]. These approaches could enhance TXD diagnostic accuracy at high-power laser facilities and thus, these approaches will be studied in the future.

Most importantly, this study shows that TXD techniques can enable single-shot retrieval of X-ray transmission and phase information from a sample using laser-driven X-ray sources in similar conditions to standard X-ray radiography diagnostics at high-power laser facilities. Additionally, in view of future developments of high repetition rate laser facilities, where data management is challenging [21], it was demonstrated that TXD diagnostic methods can provide extended information without increasing data sets volume compared to traditional absorption radiography.

Furthermore, this method also finds interest at XFEL facilities which provide enhanced X-ray probing capabilities at high repetition rates. In these experimental facilities, X-ray beam jitter can lead to phase map variations from shot to shot. The capability of self-estimating background phase and transmission signals from radiographs will enable a more systematic analysis approach that takes into account the change of X-ray source position variations, for example. This method is also compatible with optimal use of high-repetition rate beamtime capabilities while enabling lighter data sets which can speed up data analysis processes since no extra reference is needed. However, it is important to consider more sophisticated approaches in the future with advanced X-ray beam illumination and phase functions modeling considering that planar fitting may not be sufficient to accurately retrieve information from a single-image to overcome grating defects.

Acknowledgement

The authors would like to acknowledge for fundings and support: the Conseil Régional Aquitaine (INTALAX); the Agence Nationale de la Recherche (ANR- 10-IDEX-03-02, ANR-15-CE30-0011), US Department of Energy - National Nuclear Security Administration - High Energy Density Laboratory Plasmas DE-NA0001835, DE-NA0002955, and DE-NA0003882. This work has also been supported by the Research Grants No. PID2019-108764RB-I00 and PID2022-137632OB-I00 from the Spanish Ministry of Science and Innovation.

Disclosures

The authors declare no conflict of interest. The data underlying the results presented in this paper are not publicly available at this time but may be obtained from the authors upon reasonable request.

References

1. A. Snigirev, I. Snigireva, V. Kohn, S. Kuznetsov, and I. Schelokov, "On the possibilities of x-ray phase contrast microimaging by coherent high-energy synchrotron radiation," Rev. scientific instruments **66**, 5486–5492 (1995).
2. A. Momose, S. Kawamoto, I. Koyama, Y. Hamaishi, K. Takai, and Y. Suzuki, "Demonstration of x-ray talbot interferometry," Jpn. journal applied physics **42**, L866 (2003).
3. F. Pfeiffer, T. Weitkamp, O. Bunk, and C. David, "Phase retrieval and differential phase-contrast imaging with low-brilliance x-ray sources," Nat. physics **2**, 258–261 (2006).

4. L. Antonelli, F. Barbato, D. Mancelli, J. Trela, G. Zeraouli, G. Boutoux, P. Neumayer, S. Atzeni, A. Schiavi, L. Volpe, V. Bagnoud, C. Brabetz, B. Zielbauer, P. Bradford, N. Woolsey, B. Borm, and D. Batani, "X-ray phase-contrast imaging for laser-induced shock waves," Europhys. Lett. **125**, 35002 (2019).
5. A. Do, P. Troussel, S. Baton, V. Dervieux, D. Gontier, L. Lecherbourg, B. Loupias, L. Obst, F. Pérez, P. Renaudin *et al.*, "High-resolution quasi-monochromatic x-ray imaging using a fresnel phase zone plate and a multilayer mirror," Rev. Sci. Instruments **88**, 013701 (2017).
6. D. Stutman and M. Finkenthal, "Talbot-lau x-ray interferometry for high energy density plasma diagnostic," Rev. Sci. Instruments **82**, 113508 (2011).
7. J. Tang, Z. Xie, A. Du, J. Ye, Z. Zhang, J. Shen, and B. Zhou, "Design and fabrication of a ch/rf/ch tri-layer perturbation target for hydrodynamic instability experiments in icf," J. Fusion Energy **35**, 357–364 (2016).
8. R. Toth, J. Kieffer, S. Fourmaux, T. Ozaki, and A. Krol, "In-line phase-contrast imaging with a laser-based hard x-ray source," Rev. scientific instruments **76** (2005).
9. S. Kneip, C. McGuffey, F. Dollar, M. Bloom, V. Chvykov, G. Kalintchenko, K. Krushelnick, A. Maksimchuk, S. Mangles, T. Matsuoka *et al.*, "X-ray phase contrast imaging of biological specimens with femtosecond pulses of betatron radiation from a compact laser plasma wakefield accelerator," Appl. Phys. Lett. **99** (2011).
10. J. Rygg, O. Jones, J. Field, M. Barrios, L. Benedetti, G. Collins, D. Eder, M. Edwards, J. Kline, J. Kroll *et al.*, "2d x-ray radiography of imploding capsules at the national ignition facility," Phys. review letters **112**, 195001 (2014).
11. J. Soures, R. McCrory, C. Verdon, A. Babushkin, R. Bahr, T. Boehly, R. Boni, D. Bradley, D. Brown, R. Craxton *et al.*, "Direct-drive laser-fusion experiments with the omega, 60-beam,> 40 kj, ultraviolet laser system," Phys. Plasmas **3**, 2108–2112 (1996).
12. J. Zou, C. Blanc, P. Audebert, S. Janicot, A. Sautivet, L. Martin, C. Sauteret, J. Paillard, S. Jacquemot, and F. Amiranoff, "Recent progress on luli high power laser facilities," in *Journal of Physics: Conference Series,* vol. 112 (IOP Publishing, 2008), p. 032021.
13. M. L. Spaeth, K. Manes, D. Kalantar, P. Miller, J. Heebner, E. Bliss, D. Spec, T. Parham, P. Whitman, P. Wegner *et al.*, "Description of the nif laser," Fusion Sci. Technol. **69**, 25–145 (2016).
14. J. Miquel, C. Lion, and P. Vivini, "The laser mega-joule: Lmj & petal status and program overview," in *Journal of Physics: Conference Series,* vol. 688 (IOP Publishing, 2016), p. 012067.
15. I. A. Begishev, V. Bagnoud, S.-W. Bahk, W. Bittle, G. Brent, R. Cuffney, C. Dorrer, D. Froula, D. Haberberger, C. Mileham *et al.*, "Advanced laser development and plasma-physics studies on the multiterawatt laser," Appl. Opt. **60**, 11104–11124 (2021).
16. H. F. Talbot, "Lxxvi. facts relating to optical science. no. iv," The London, Edinburgh, Dublin Philos. Mag. J. Sci. **9**, 401–407 (1836).
17. L. Rayleigh, "Xxv. on copying diffraction-gratings, and on some phenomena connected therewith," The London, Edinburgh, Dublin Philos. Mag. J. Sci. **11**, 196–205 (1881).
18. J. Ojeda-Castañeda, J. Ibarra, and J. C. Barreiro, "Noncoherent talbot effect: coherence theory and applications," Opt. Commun. **71**, 151–155 (1989).
19. E. Lau, "Beugungserscheinungen an doppelrastern," Ann. der Physik **437**, 417–423 (1948).
20. G. Pérez-Callejo, V. Bouffetier, L. Ceurvorst, T. Goudal, M. P. Valdivia, D. Stutman, and A. Casner, "TIA: A forward model and analyzer for Talbot interferometry experiments of dense plasmas," Phys. Plasmas **29**, 043901 (2022).
21. G. Pérez-Callejo, V. Bouffetier, L. Ceurvorst, T. Goudal, S. R. Klein, D. Svyatskiy, M. Holec, P. Perez-Martin, K. Falk, A. Casner, T. E. Weber, G. Kagan, and M. P. Valdivia, "Phase imaging of irradiated foils at the omega ep facility using phase-stepping x-ray talbot–lau deflectometry," High Power Laser Sci. Eng. **11**, e49 (2023).
22. A. Momose, W. Yashiro, Y. Takeda, Y. Suzuki, and T. Hattori, "Phase tomography by x-ray talbot interferometry for biological imaging," Jpn. journal applied physics **45**, 5254 (2006).
23. M. P. Valdivia, F. Veloso, D. Stutman, C. Stoeckl, C. Mileham, I. A. Begishev, W. Theobald, M. Vescovi, W. Useche, S. P. Regan, B. Albertazzi, G. Rigon, P. Mabey, T. Michel, S. A. Pikuz, M. Koenig, and A. Casner, "X-ray backlighter requirements for refraction-based electron density diagnostics through talbot-lau deflectometry," Rev. Sci. Instruments **89**, 10G127 (2018).
24. C. Walsh, J. Sadler, and J. Davies, "Updated magnetized transport coefficients: Impact on laser-plasmas with self-generated or applied magnetic fields," Nucl. Fusion **61**, 116025 (2021).
25. J. R. Davies, "Nonlocal suppression of biermann battery magnetic-field generation for arbitrary atomic numbers and magnetization," Phys. Plasmas **30** (2023).
26. M. Fiddy, "The phase retrieval problem," in *Inverse Optics I,* vol. 413 (SPIE, 1983), pp. 176–181.
27. M. Chabior, T. Donath, C. David, M. Schuster, C. Schroer, and F. Pfeiffer, "Signal-to-noise ratio in x ray dark-field imaging using a grating interferometer," J. applied physics **110** (2011).
28. M. P. Valdivia, D. Stutman, C. Stoeckl, C. Mileham, I. A. Begishev, J. Bromage, and S. P. Regan, "Talbot–lau x-ray deflectometry phase-retrieval methods for electron density diagnostics in high-energy density experiments," Appl. Opt. **57**, 138–145 (2018).
29. D. Stutman, M. P. Valdivia, and M. Finkenthal, "X-ray moiré deflectometry using synthetic reference images," Appl. optics **54**, 5956–5961 (2015).
30. F. Condamine, N. Jourdain, D. Kramer, P. Trojek, A. Gintrand, G. Fauvel, P. Pandikian, J. Bartoníček, G. Friedman, M. Havlík *et al.*, "Commissioning results from the high-repetition rate nanosecond-kilojoule laser beamline at the extreme light infrastructure," Plasma Phys. Control. Fusion **65**, 015004 (2022).

31. U. Zastrau, K. Appel, C. Baehtz, O. Baehr, L. Batchelor, A. Berghäuser, M. Banjafar, E. Brambrink, V. Cerantola, T. E. Cowan *et al.*, "The high energy density scientific instrument at the european xfel," J. synchrotron radiation **28**, 1393–1416 (2021).
32. M. Makita, G. Seniutinas, M. H. Seaberg, H. J. Lee, E. C. Galtier, M. Liang, A. Aquila, S. Boutet, A. Hashim, M. S. Hunter *et al.*, "Double grating shearing interferometry for x-ray free-electron laser beams," Optica **7**, 404–409 (2020).
33. Y. Liu, M. Seaberg, Y. Feng, K. Li, Y. Ding, G. Marcus, D. Fritz, X. Shi, W. Grizolli, L. Assoufid *et al.*, "X-ray free-electron laser wavefront sensing using the fractional talbot effect," J. Synchrotron Radiat. **27**, 254–261 (2020).
34. V. Bouffetier, "Développement de l'interférométrie x et application à l'imagerie par contraste de phase de plasmas denses et turbulents," Ph.D. thesis, Bordeaux (2021).
35. V. Cerantola, A. D. Rosa, Z. Konôpková, R. Torchio, E. Brambrink, A. Rack, U. Zastrau, and S. Pascarelli, "New frontiers in extreme conditions science at synchrotrons and free electron lasers," J. Physics: Condens. Matter **33**, 274003 (2021).
36. T. Donath, M. Chabior, F. Pfeiffer, O. Bunk, E. Reznikova, J. Mohr, E. Hempel, S. Popescu, M. Hoheisel, M. Schuster *et al.*, "Inverse geometry for grating-based x-ray phase-contrast imaging," J. Appl. Phys. **106**, 054703 (2009).
37. T. Weitkamp, "Xwfp: An x-ray wavefront propagation software package for the idl computer language," in *Advances in Computational Methods for X-Ray and Neutron Optics,* vol. 5536 (SPIE, 2004), pp. 181–189.
38. T. Weitkamp, A. Diaz, C. David, F. Pfeiffer, M. Stampanoni, P. Cloetens, and E. Ziegler, "X-ray phase imaging with a grating interferometer," Opt. express **13**, 6296–6304 (2005).
39. V. Bouffetier, L. Ceurvorst, M. Valdivia, F. Dorchies, S. Hulin, T. Goudal, D. Stutman, and A. Casner, "Proof-of-concept talbot–lau x-ray interferometry with a high-intensity, high-repetition-rate, laser-driven k-alpha source," Appl. optics **59**, 8380–8387 (2020).
40. M. P. Valdivia, G. Perez-Callejo, V. Bouffetier, G. W. Collins, C. Stoeckl, T. Filkins, C. Mileham, M. Romanofsky, I. A. Begishev, W. Theobald, S. R. Klein, M. K. Schneider, F. N. Beg, A. Casner, and D. Stutman, "Current advances on talbot–lau x-ray imaging diagnostics for high energy density experiments (invited)," Rev. Sci. Instruments **93**, 115102 (2022).
41. L. Jarrott, M. Wei, C. McGuffey, F. Beg, P. Nilson, C. Sorce, C. Stoeckl, W. Theoboald, H. Sawada, R. Stephens *et al.*, "Calibration and characterization of a highly efficient spectrometer in von hamos geometry for 7-10 kev x-rays," Rev. Sci. Instruments **88**, 043110 (2017).
42. W. Theobald, V. Ovchinnikov, S. Ivancic, B. Eichman, P. M. Nilson, J. A. Delettrez, R. Yan, G. Li, F. J. Marshall, D. D. Meyerhofer, J. F. Myatt, C. Ren, T. C. Sangster, C. Stoeckl, J. D. Zuegel, L. Van Woerkom, R. R. Freeman, K. U. Akli, E. Giraldez, and R. B. Stephens, "High-intensity laser-plasma interaction with wedge-shaped-cavity targets," Phys. Plasmas **17**, 103101 (2010).
43. R. Stephens, R. Snavely, Y. Aglitskiy, F. Amiranoff, C. Andersen, D. Batani, S. Baton, T. Cowan, R. Freeman, T. Hall *et al.*, "K α fluorescence measurement of relativistic electron transport in the context of fast ignition," Phys. Rev. E **69**, 066414 (2004).
44. C. Huntington, C. Krauland, C. Kuranz, R. Drake, H.-S. Park, D. Kalantar, B. Maddox, B. Remington, and J. Kline, "Development of a short duration backlit pinhole for radiography on the national ignition facility," Rev. Sci. Instruments **81** (2010).
45. A. Morace, L. Fedeli, D. Batani, S. Baton, F. Beg, S. Hulin, L. Jarrott, A. Margarit, M. Nakai, M. Nakatsutsumi *et al.*, "Development of x-ray radiography for high energy density physics," Phys. Plasmas **21** (2014).
46. F. Barbato, S. Atzeni, D. Batani, D. Bleiner, G. Boutoux, C. Brabetz, P. Bradford, D. Mancelli, P. Neumayer, A. Schiavi *et al.*, "Quantitative phase contrast imaging of a shock-wave with a laser-plasma based x-ray source," Sci. reports **9**, 18805 (2019).
47. P. Zhu, K. Zhang, Z. Wang, Y. Liu, X. Liu, Z. Wu, S. A. McDonald, F. Marone, and M. Stampanoni, "Low-dose, simple, and fast grating-based x-ray phase-contrast imaging," Proc. National Acad. Sci. **107**, 13576–13581 (2010).
48. D. Paganin, *Coherent X-ray optics* (Oxford University Press, USA, 2006), chap. Chapter 4: Coherent X-ray imaging, pp. 240–300, 6.
49. H.-S. Park, D. Chambers, H.-K. Chung, R. Clarke, R. Eagleton, E. Giraldez, T. Goldsack, R. Heathcote, N. Izumi, M. Key *et al.*, "High-energy k α radiography using high-intensity, short-pulse lasers," Phys. plasmas **13**, 056309 (2006).
50. M. Valdivia, D. Stutman, C. Stoeckl, C. Mileham, J. Zou, S. Muller, K. Kaiser, C. Sorce, P. Keiter, J. Fein *et al.*, "Implementation of a talbot–lau x-ray deflectometer diagnostic platform for the omega ep laser," Rev. Sci. Instruments **91**, 023511 (2020).
51. J. Workman, J. R. Fincke, G. A. Kyrala, and T. Pierce, "Uniform large-area x-ray imaging at 9 kev using a backlit pinhole," Appl. optics **44**, 859–865 (2005).
52. M. Hill, G. Williams, A. Zylstra, C. Stan, T. Lockard, E. Gumbrell, R. Rudd, P. Powell, D. Swift, J. McNaney *et al.*, "High resolution> 40 kev x-ray radiography using an edge-on micro-flag backlighter at nif-arc," Rev. Sci. Instruments **92**, 033535 (2021).
53. G. Arthur and C. Spindloe, "Fabrication of mass produced microdot arrays for use as micro-targets on high-repetition rate experiments." CLF Annu. Report,(2011-2012) (2012).